Journal of Materials Science & Technology 182 (2024) 165–175

Contents lists available at ScienceDirect

Journal of Materials Science & Technology

journal homepage: www.elsevier.com/locate/jmst

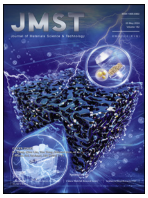

Research Article

Annealing cracking in Zr and a Zr-alloy with low hydrogen concentration

Xi-Heng Lin[a], Irene J. Beyerlein[b,c,*], Wei-Zhong Han[a,*]

[a] *Center for Advancing Materials Performance from the Nanoscale, State Key Laboratory for Mechanical Behavior of Materials, Xi'an Jiaotong University, Xi'an 710049, China*
[b] *Materials Department, University of California, Santa Barbara, CA 93106-5070, USA*
[c] *Department of Mechanical Engineering, University of California, Santa Barbara, CA 93106-5070, USA*

ARTICLE INFO

Article history:
Received 26 August 2023
Revised 11 September 2023
Accepted 12 September 2023
Available online 18 November 2023

Keywords:
Zirconium
Hydride
Cracking
Habit plane
Reorientation

ABSTRACT

Hydrogen embrittlement, also known as hydrogen-induced cracking, is a longstanding concern for zirconium (Zr) and its alloys. The affinity for hydrogen in zirconium results in the formation of brittle hydrides. Hydrides are conventionally thought to facilitate crack propagation, and the prevailing recommendation to hinder hydride embrittlement involves reducing the hydrogen concentration in the material and applying slow cooling to reduce thermal stresses. Here, in Zr with a maximum hydrogen concentration of 43 wppm, we show that cracks initiate unexpectedly after annealing, a step that involves slow cooling and no external stress. With a suite of high-resolution microscopy, we show that annealing cracks initiate at prismatic δ-hydrides, whose presence is unexpected. The microscopic annealing crack paths are consequently crystallographic, following the habit plane of these prismatic δ-hydrides. The commonly reported γ-hydride and δ-hydrides that develop on the basal plane are found not to initiate cracks. We rationalize that prismatic δ hydrides result from the intergranular thermal residual stresses that develop during slow cooling. This finding of uncommon annealing cracking further advances the mechanistic understanding of hydride embrittlement in zirconium and can lead to new strategies for design and fabrication of advanced zirconium alloys for harsh environments.

1. Introduction

Hydrogen-induced cracking occurs in many metals and alloys, causing serious safety issues and losses in operating time and significant costs every year [1,2]. Zirconium (Zr) alloys are used extensively as structural components in nuclear reactors as fuel claddings and pressure tubes due to their low thermal neutron absorption and corrosion resistance. Zr has a strong affinity for hydrogen, and second phases, known as hydrides, precipitate easily once the solid solubility of hydrogen is exceeded [3–5]. These brittle hydrides can degrade material toughness and enhance the propensity for cracking [5–7]. Identifying the embrittlement mechanisms of hydrides is critical for production efficiency and in-reactor performance of Zr components.

The conventional explanation for the embrittling effect of hydrides is the formation of radial hydrides, hydrides that are aligned with the radius of the cladding or pressure tube. Radial hydrides can substantially degrade toughness and lead to through-wall fractures [6,8]. They facilitate the propagation of microcracks that may have formed from thermomechanical stresses [6–8]. Initially, hydrides are, however, circumferential hydrides, which have a minor effect on the mechanical property degradation of Zr components compared to their radial hydride counterpart [9–12]. The radial hydrides form because of a process referred to as hydride "reorientation" when the tubes are cooled down while under a relatively high hydrogen concentration (about 50–700 wppm) and/or high stress environment [7]. The morphological change from the circumferential to radial orientation involves initial circumferential hydride dissolution at high temperature and a reprecipitation into radial hydrides when cooled to room temperature, while under sufficiently high tensile hoop stresses, due to either external or residual stresses [5]. Based on this understanding, the recommended practice is to slowly cool crack-free Zr components with low hydrogen concentration and under no stresses. This step has since become an indispensable step in the processing and production of various Zr components. Although crack initiation at radial hydrides was commonly observed [11–13], however, whether and,

---

* Corresponding authors.

E-mail addresses: beyerlein@ucsb.edu (I.J. Beyerlein), wzhanxjtu@mail.xjtu.edu.cn (W.-Z. Han).

https://doi.org/10.1016/j.jmst.2023.09.039

Table 1
Chemical composition of the as-received high-purity Zr (wt%).

Hf	Fe	Si	Sn	Ni	Cr	O	C	H
$\leq$ 0.001	$\leq$ 0.002	$\leq$ 0.001	$\leq$ 0.0005	$\leq$ 0.0007	$\leq$ 0.008	$\leq$ 0.014	$\leq$ 0.001	$\approx$ 0.0007

Table 2
Chemical composition of the Zr-Sn-Nb-Fe alloy tubes used in the present work (wt%).

Sn	Nb	Fe	Zr
1.0	1.0	0.1	Balance

if so how, reoriented hydrides participate in crack initiation in the crack-free materials remains unknown.

In addition to the morphological orientation, hydrides also vary in crystallographic orientation. In the absence of stress, hydrides preferentially precipitate on the basal plane of the hexagonal close packed (HCP) Zr matrix (α-Zr) [14–18], but under stress, they can adopt one of several possible habit planes, i.e., the $\{10\bar{1}i\}$ planes, where $i = 0$–7 [19–21]. Although the effect of stress on hydride habit plane has been explored to some extent, there is still a lack of direct experimental evidence to support the correlation between hydride habit plane selection and crack initiation.

In this work, we investigated an unexpected subsurface cracking while annealing pure Zr and a Zr-Sn-Nb-Fe alloy with low hydrogen concentration, under a slow cooling mode, and without applying external stress. We find that the slow cooling rate generates hydrides that adopt an uncommon habit plane, aligned with the $\{10\bar{1}0\}$ prismatic plane of Zr. We show that these prismatic hydrides are the origin of annealing cracks. Further, the annealing crack propagation pathways are crystallographic and dictated by the location of the prismatic hydrides. It is rationalized that these uncommon hydrides developed with the assistance of intergranular thermal residual stresses that reach sufficiently high levels because of the anisotropic coefficient of thermal expansion of Zr. The findings here reveal an underlying crack initiating mechanism of hydrogen embrittlement and demonstrate a direct connection between crack initiation with hydride habit plane.

2. Materials and methods

2.1. Sample preparation for annealing

High-purity Zr (99.99 %) and Zr-Sn-Nb-Fe alloys were used in this study, see Tables 1 and 2 for their compositions. The Type-I and Type-II test samples of the Zr-Sn-Nb-Fe alloy were drawn from the tubular material at different stages in mechanical processing. Bulk samples with dimensions of 10/14 mm × 6.5 mm × 8.5 mm along length (LD), width (TD) and thickness (ND) directions were cut from the as-received pure Zr plate and Zr-Sn-Nb-Fe alloy tubes (the diameter and wall thickness of the tube is 86 mm and 13 mm, respectively). Before annealing, the samples were mechanically ground with 80, 220 and 600 grit waterproof abrasive paper to gain a smooth and flat surface. To avoid being contaminated by air or being oxidized, specimens subjected to all heat treatments were sealed in an alundum tubular furnace (GSL-1400X) with a vacuum of about 3×10^{-4} Pa. For furnace-cooled to room temperature (RT), the samples were held under high vacuum in furnace during the entire heat-treatment. For air-cooled or water-quenched to RT, the samples were first heated and held to high temperature under vacuum in furnace, and then taken out of furnace and cooled in ambient air or ultrapure water.

Before annealing, the initial hydrogen concentration of the as-received pure Zr and Zr-Sn-Nb-Fe alloy specimens is about 7 wppm (LECO hydrogen analyzer RH600, GB/T 13747.21-2017, the testing error range is ±4 wppm). After the high-vacuum annealing in furnace, the hydrogen concentration is about 8 wppm, which indicates that the annealing process will not alter the hydrogen concentration.

2.2. Microstructure characterizations

For all specimens requiring scanning electron microscopy (SEM, SU6600) and electron backscattered diffraction (EBSD) characterizations (including the as-received and annealed samples), the same surface treatment was used to exclude the possible influence of the sample preparation method on hydride formation and cracking. Thin slices with a thickness of 0.7 mm were firstly cut from the bulk sample (for both the as-received and annealed samples). As for annealed specimens, thin slices with a thickness of 0.7 mm were sampled at different positions along the thickness direction of the block to gain the gradient distribution of cracks. The slices were then mechanically ground with 80, 220 and 600 grit waterproof abrasive paper to about 0.2 mm in thickness. Finally, they were polished by twin-jet electro-polishing in a solution of 10% perchloric acid and 90% ethanol to remove the surface oxide layer and stress layer. The electrolyte temperature was maintained at −40 °C, and the voltage set to about 25 V. The number density and length of cracks in all samples used for statistics were obtained based on sixteen 600× SEM images (209 μm × 146 μm) and averaged. EBSD patterns were obtained and analyzed by means of the Aztec HKL software, with a voltage of 25 kV and probe current of 2.7 nA. Samples for transmission electron microscopy (TEM, JEOL 2100F) characterization were cut at the crack via the focus ion beam (FIB) sample-lifting technique. A focused Ga+ ion beam (at an acceleration voltage of 30 kV) was used to slice the electron transparent lamella. A micro-manipulation lift-out system (FEI Helios Nanolab600) was used to transport the lamella. The microstructures of the hydrides on the lifted-out plane were characterized using TEM with an acceleration voltage of 200 kV.

The sample preparation methods including mechanical grinding, electro-polishing or FIB processing can easily induce artificial hydrides in the material. However, the concentration of hydride introduced during sample preparation is very low and these hydrides usually grow parallel to the basal plane [22]. No δ hydride bundles were detected in the as-received samples using the current same sample preparation methods. Therefore, the current sample preparation methods for microstructure characterizations will not introduce an additional uncertainty to the results.

2.3. Electrolytic hydrogen charging

Pure Zr with the initial hydrogen concentration of about 7 wppm was used in this study. Hydrogen charging of the pure Zr samples was carried out electrochemically in a solution of 0.5 mol/L sulfuric acid using a current density of 0.2 A/cm^2 at RT for different times (see details Table 3). After hydrogen charging, the samples were annealed at 600 °C for 1 h then followed by a slow furnace cooling to RT in high vacuum to homogenize the hydrogen distribution and to form hydrides. The hydrogen concentration of the test specimens, including the as-received, 10 min and

Table 3
Electrolytic hydrogen charging parameters. Pure Zr samples hydrogen-charged for 10 and 30 min are denoted as Zr-H10 and Zr-H30, respectively.

Specimen	Electrolyte solution	Current density (A/cm^2)	Electrolyte temperature	Charging time (min)	Hydrogen concentration (wppm)
Pure Zr (Zr-H10)	0.5 mol/L sulfuric acid	0.2	RT	10	20
Pure Zr (Zr-H30)	0.5 mol/L sulfuric acid	0.2	RT	30	43

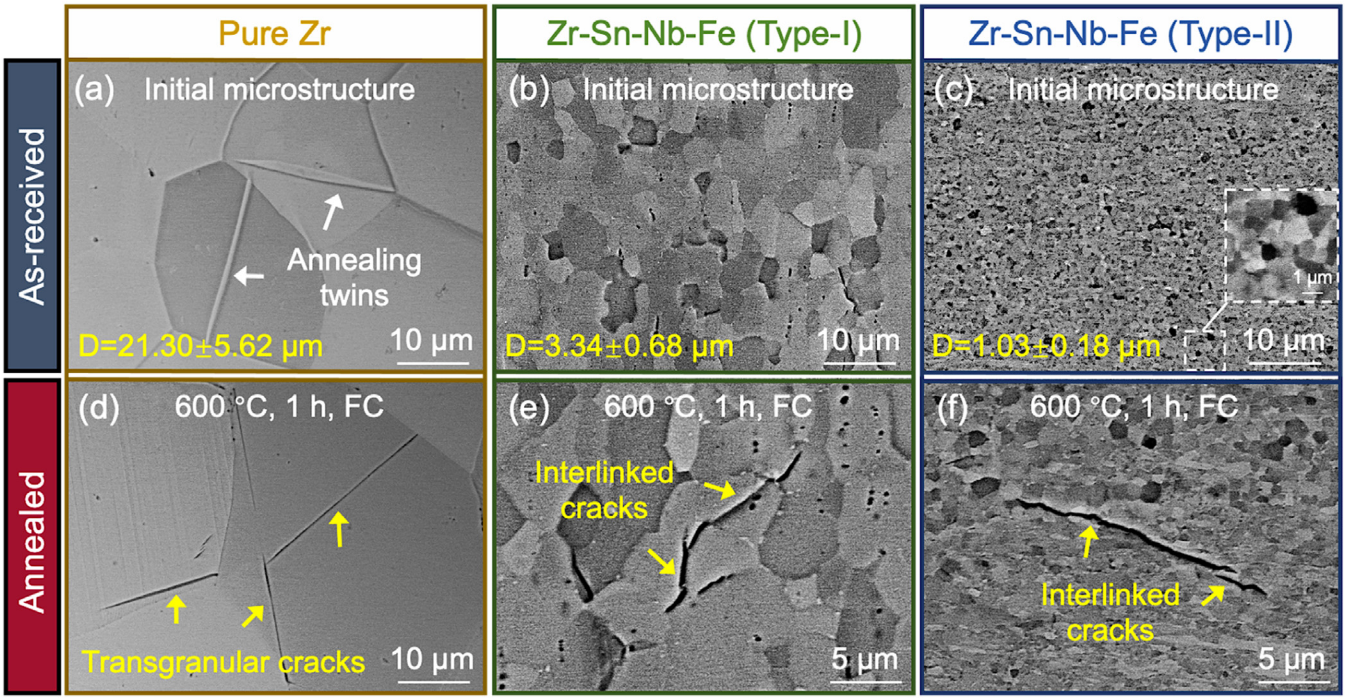

Fig. 1. Annealing cracking in pure Zr and the Zr-Sn-Nb-Fe alloys. (a–c) Initial grain structures in pure Zr and the Zr-Sn-Nb-Fe alloys. The Type-I and Type-II Zr-Sn-Nb-Fe alloys have the same chemical compositions but different grain sizes. (d-f) Cracks in the sub-surface layer of bulk samples after annealing at 600 °C for 1 h and furnace-cooled (FC) down to room temperature. Micro-scale cracks are marked with yellow arrows.

30 min hydrogen-charged pure Zr samples, was determined by the LECO hydrogen analyzer RH-600. The hydrogen concentrations in two electrochemically charged samples are 20 wppm (10 min) and 43 wppm (30 min), respectively (Table 3).

3. Results

3.1. Microstructures of the annealed Zr and Zr-Sn-Nb-Fe

High vacuum annealing treatments were employed to process both pure Zr and two types of Zr-Sn-Nb-Fe alloys (denoted as Type-I and Type-II). These alloys are used in application and are included since alloying can affect hydrogen absorption [5]. Before annealing, the pure Zr and the Zr-Sn-Nb-Fe alloy specimens were naturally exposed to air and initially have a hydrogen concentration of about 7 wppm. They were then annealed in high vacuum furnace followed by slow cooling to RT from an elevated temperature (600 °C) under no external stress, conditions designed to prevent cracking. Fig. 1 compares the secondary electron (SE) mode SEM images of their initial and annealed microstructures. All samples have equiaxed grains but different grain sizes, as shown in Fig. 1(a)–(c). After annealing at 600 °C for 1 h and furnace-cooling (FC) to RT, microscale cracks are detected below the surface, within about 3 mm from the top surface, of all samples (Fig. 1(d)–(f)). To eliminate the possibility of material removal caused by electropolishing, a combined technique of mechanical polishing and vibration polishing were used to polish the as-annealed pure Zr sample. Similar cracking traces were also observed. The number density of cracks decreases nonlinearly from the sample surface to the central part (supplementary material, Fig. S1). In the coarse-grained pure Zr, transgranular cracks initiate at the grain boundaries (GBs), and then extend into the grain interior, as shown in Fig. 1(d). In the fine-grained Zr-Sn-Nb-Fe samples, cracking also occurs but in the form of an interlinked crack network composed of transgranular and intergranular cracks across several grains (Fig. 1(e) and (f)). These cracks are unexpected since the annealing step is intended to relieve residual stress and minimize crack formation.

3.2. Influencing factors of annealing cracking

The annealing step involves many variables, any one of which could have caused cracking during annealing. To identify them, we considered four possible factors: heating rate (V_h), annealing temperature (T_a), holding time (t_h) and cooling rate (V_c) (see Table 4 for summary). As each is varied, the other three are held fixed, and for each case, the crack number density and length are measured within 0.7 mm from the top-surface of all samples (as shown in Fig. 2(a)–(d)). Under FC, as used earlier, but with either heating rate, annealing temperature or holding time varied, annealing cracking still occurred (Fig. 2(a)–(c)). Further, the number density

Table 4
Summary of annealing conditions for pure Zr and the Zr-Sn-Nb-Fe alloys. The effects of heating rate (V_h), annealing temperature (T_a), holding time (t_h) and cooling rate (V_c) on annealing cracking are analyzed in pure Zr with four groups of samples (denoted as I, II, III and IV). For group II, the annealing temperatures chosen ranged from low temperatures around 300 °C to high-temperatures below the phase transformation temperature (about 862 °C). Annealing experiments at 600 °C via FC were repeated for hydrogenated Zr (including Zr-H10 and Zr-H30) and Zr-Sn-Nb-Fe alloys.

Specimen		V_h (°C/min)	T_a (°C)	t_h (h)	V_c (°C/min)
Pure Zr	I	3, 10, 15	600	1	10 (FC)
	II	10	300, 350, 400, 500, 550, 600, 650, 700, 750, 800, 850	1	10 (FC)
	III	10	600	0, 1, 5	10 (FC)
	IV	10	600	1	3 (SFC), 10 (FC), >720 (AC), >6 × 10^4 (WQ)
Zr-Sn-Nb-Fe (Type-I)		10	600	1	10 (FC)
Zr-Sn-Nb-Fe (Type-II)		10	600	1	10 (FC)
Hydrogenated Zr		10	600	1	10 (FC)

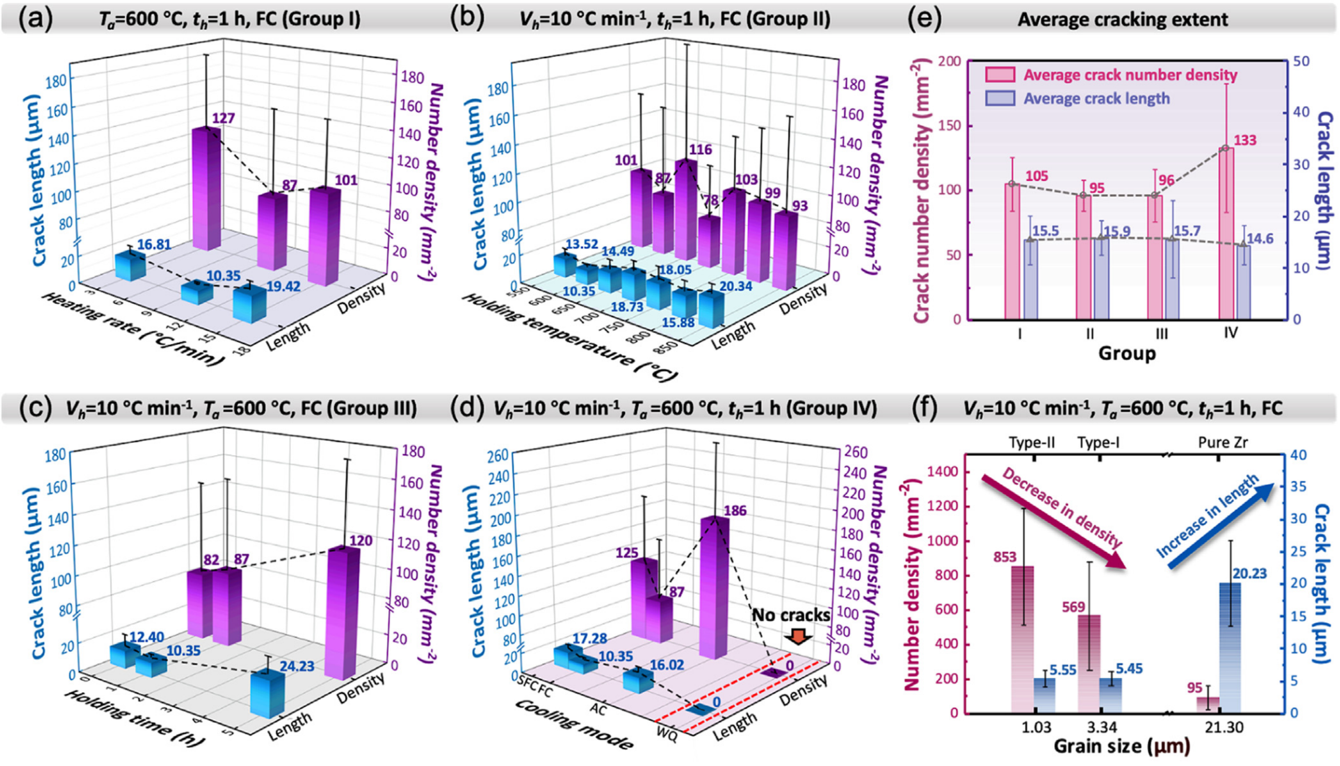

Fig. 2. Influence of annealing conditions and grain size on cracking. (a) Heating rate vs. cracking. (b) Annealing temperature vs. cracking. (c) Holding time vs. cracking. (d) Cooling rate vs. cracking. (e) The effect of annealing condition on microstructure cracking in pure Zr. Samples that are water-quenched (WQ) to RT are excluded from Group IV here. (f) Cracking extent vs. grain size. The error bars are due to the non-uniform distribution of cracks.

and length of the annealing cracks negligibly varied (Fig. 2(a)–(c)). The fourth variable (Fig. 2(d)), cooling rate (V_c), is designed to range from slower to faster than that previously used: (1) slow furnace cooling (SFC, V_c = 3 °C/min), (2) furnace cooling (FC, V_c = 10 °C/min), as before, (3) air cooling (AC, V_c >720 °C/min) and 4) water quenching (WQ, V_c >6 × 10^4 °C/min). Under the three slower cooling rates (i.e., SFC, FC, AC), annealing cracks were again unexpectedly seen to form and moreover, their crack densities vary negligibly among these rates (Fig. 2(d)). The amount of cracking is noticeable. In pure Zr, for instance, the average number density of cracks is about 107 mm^{-2} and the average crack length about 15.4 μm (Fig. 2(e)). Significantly, among all cases, the WQ Zr samples were free of annealing cracks (Fig. 2(d)). The WQ Zr-Sn-Nb-Fe alloy samples were also free of detectable cracks. This is another unexpected outcome. Faster cooling rates are anticipated to facilitate crack initiation, not suppress it, due to larger thermal gradients and residual stresses generated, and hence are usually avoided [23,24].

With the same annealing treatment, grain size also influenced crack properties but did not prevent cracking (Fig. 2(f)). As grain size increased, the crack number density decreases while the crack length increases.

3.3. Crystallographic feature of cracking

3.3.1. Cleavage cracking and δ-hydrides

Towards an explanation, microscopic analysis is conducted on pure Zr samples that underwent annealing and slow cooling to determine the origin of the cracks. As shown in Fig. 3, EBSD scans are shown of typical cracked regions within grains of pure Zr, annealed at 600 °C and 850 °C, respectively for 1 h and then furnace-cooled to RT. At this scale, fine microscopic hydrides can be seen. These

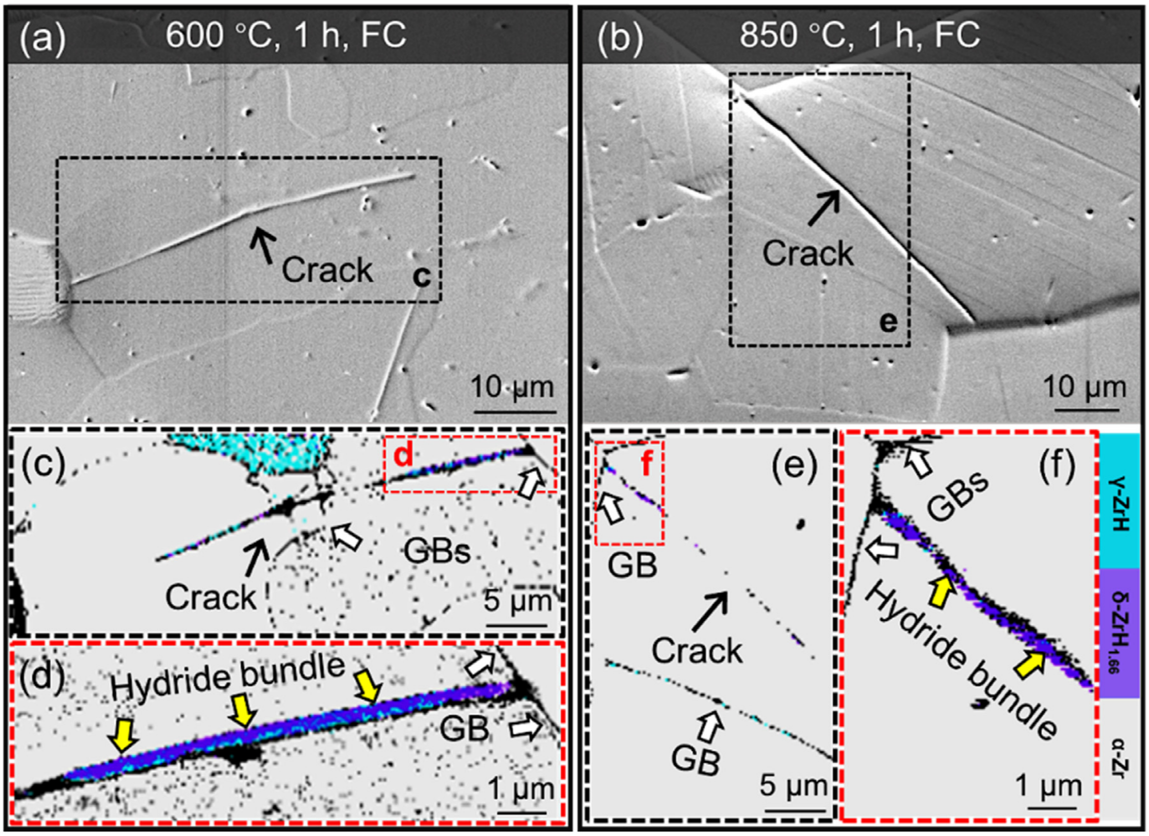

Fig. 3. Annealing cracking and hydrides precipitation in annealed pure Zr. (a) and (b) Secondary electron SEM images of the cracks under different annealing conditions. (c) and (e) Phase maps (with step size of 0.5 μm) of the regions are outlined by a black-dotted box in (a) and (b). The α-Zr is colored in gray, the δ hydride (δ-$ZrH_{1.66}$) in purple and the γ hydride (γ-ZrH) in light blue. (d) and (f) Enlarged images (with step size of 0.02 μm) of the cracks marked with red dash boxes in (c) and (e). Hydrides (hydride bundles) are highlighted with yellow arrows.

were not present in the initial samples and were precipitated during the annealing treatment. It is well known that the solubility of hydrogen in Zr decreases rapidly with temperature, being as low as 1 wppm at RT [3,5]. Therefore, precipitation of hydrides is not entirely unexpected during slow cooling from high temperature. Yet, in practice, cracking from hydride formation is believed to be hindered in little to no external stress, hydrogen-dilute environments.

As shown in Fig. 3(c), (d) and (f), two hydride variants can be identified—a face-centered cubic (FCC) δ-hydride ($ZrH_{1.66}$) and a face-centered tetragonal (FCT) γ-hydride ($ZrH_{1.0}$) [5]. The δ-hydrides initiate at GBs and grow into grain interior, while the γ-hydrides are in dispersed distribution. These two hydride phases have been reported in Zr and Zr alloys in numerous studies, usually under hydrogen-concentrations [5–8]. The δ-hydride is the most frequently seen hydride to form in Zr components, either during fabrication or in-service. It is the stable phase that forms via diffusional phase transformation and thereby favored to form under slow cooling [25]. The γ-phase is a meta-stable phase and is the product of martensitic shear transformation [26]. It not as frequently seen and favored to form after fast cooling (e.g., WQ) [5,6]

The analysis finds that cracks are related to the δ-hydrides. Many of the δ-hydrides aggregate inside the cracks to form a layered hydride bundle (Fig. 3(d) and (f)). These δ-hydride bundles are thickest at the GBs and thinnest in the grain interior. Likewise, the cracks associated with the bundles, appear thicker at the GBs. The correspondence suggests that the δ-hydride bundles and cracks nucleated at GBs and grew into the grain interior. In most cases, the cracks are confined to one grain (see Fig. 3(b) and supplementary material, Fig. S2(a)). Although not as frequently seen, some cracks propagated across the GBs and span multiple grains (Fig. 3(c) and supplementary material, Fig. S2(b)). In contrast, the γ-hydrides are unrelated to cracking (see Fig. 3(c) and supplementary material, Fig. S3).

In the annealed Zr-Sn-Nb-Fe (Type-II) alloy, long cracks extending across several grains are detected (Fig. 4). Multiple δ-hydride bundles are observed inside these cracks, and the δ-hydride bundles in different grains form a long chain of δ-hydrides (Fig. 4(b) and (e)). Like crack nucleation, crack propagation in Zr-Sn-Nb-Fe alloy also proceeds nearly parallel to a chain of δ-hydride bundles.

3.3.2. Orientation relationship (OR) and habit plane of the cracking related δ-hydrides

Crack initiation at such fine scale δ-hydrides is not anticipated, particularly when the hydride/Zr interface experiences no stress or pressure, which is the situation here. To help explain the observations, we analyzed the crystallography of the hydride/Zr interface. Fig. 5(a) shows the crystallographic orientation for the δ-hydride bundle and the cracked Zr matrix. Pole figures in Fig. 5(b) and (c) indicate a predominant OR of $(0001)_{\alpha\text{-Zr}}//\{001\}_{\delta}$, $<11\bar{2}0>_{\alpha\text{-Zr}}//<110>_{\delta}$ and $<10\bar{1}0>_{\alpha\text{-Zr}}//<110>_{\delta}$. The habit plane trace of the δ-hydride bundle (indicated by black line in $<10\bar{1}0>_{\alpha\text{-Zr}}$ pole figure in Fig. 5(b)) is parallel to one of the $\{10\bar{1}0\}$ prismatic planes of α-Zr (see white dotted line in Fig. 5(a)). This prismatic interface plane is uncommon and arguably rare for δ-hydrides, as most studies report the basal plane of α-Zr as the habit plane [18–21]. The basal plane results in a relatively low lattice misfit with the δ-hydride and interface energy and hence this plane is an established characteristic of δ-hydrides [27]. To distinguish the δ-hydride bundles with a $\{10\bar{1}0\}$ habit plane seen here, we refer to them as *prismatic hydrides*, and the common δ-hydrides

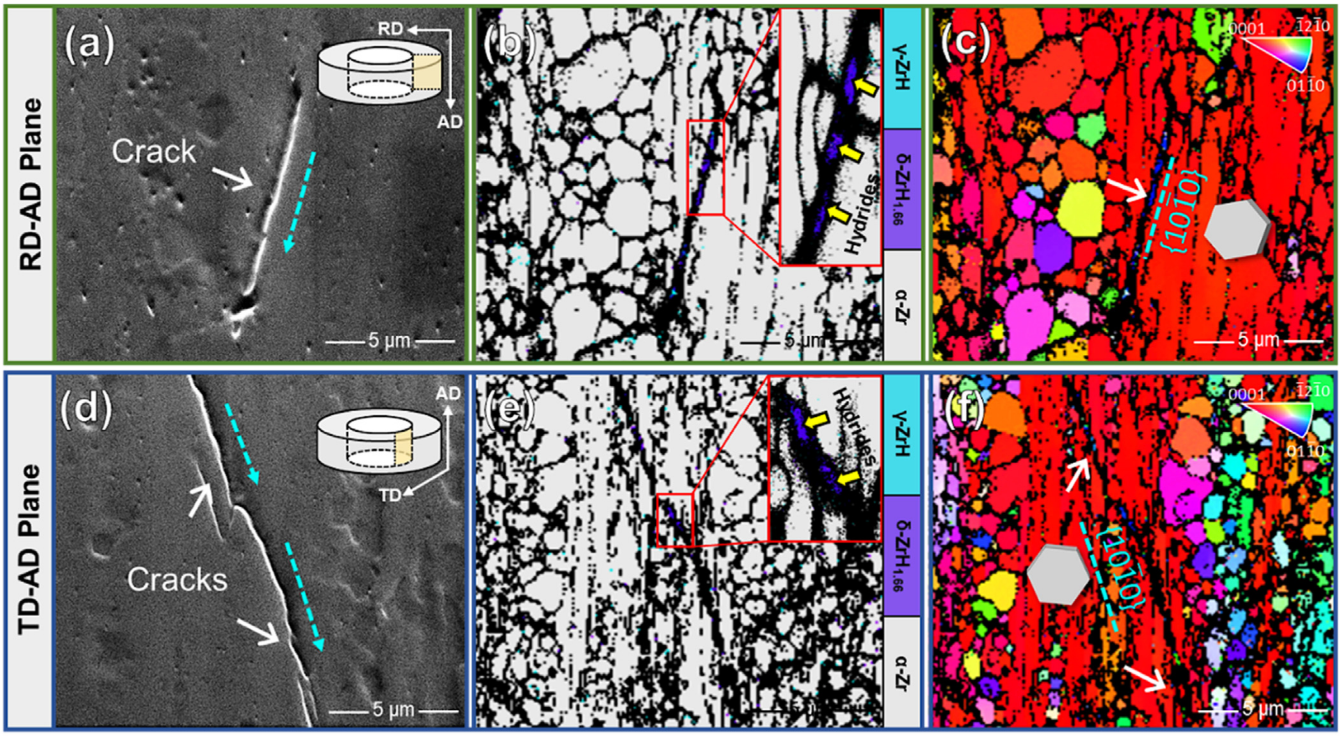

Fig. 4. Annealing cracking in Zr-Sn-Nb-Fe (Type-II) viewed from different directions. (a) and (d) SEM images of annealing cracking in the radial (RD)-axial (AD) plane and tangential or circumferential (TD)-axial (AD) plane of the tube sample. The RD-AD plane and TD-AD plane are shown in the tube model and colored in yellow. Cracks are marked with white arrows and cracking directions are marked with light blue dotted arrows. (b) and (e) Phase maps. Hydrides inside the cracks are enlarged in the red rectangles and highlighted by yellow arrows. (c) and (f) Crystal orientation maps. Orientations of profuse Zr grains around the cracks are consistent due to their strong texture. $\{10\bar{1}0\}$ prismatic planes are indicated by light-blue dotted lines.

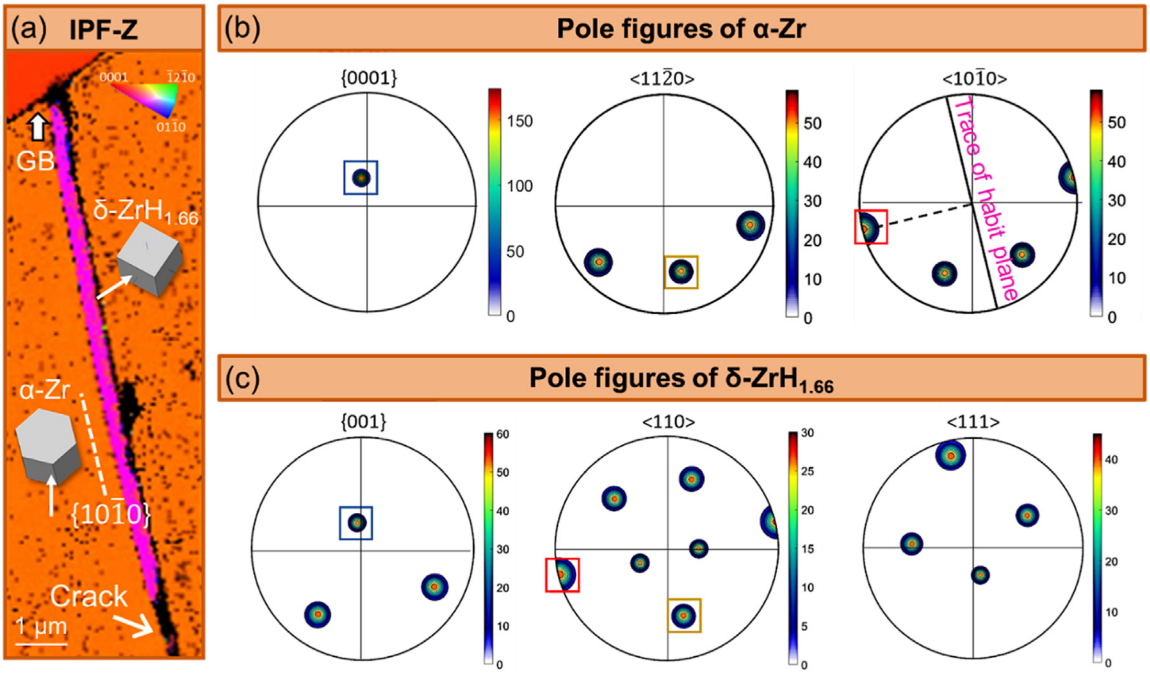

Fig. 5. Crystallographic character of δ-hydrides and cracking. (a) Inverse pole figure (IPF-Z) map (with step size of 0.02 μm) of an annealing crack and δ-hydrides. (b) and (c) Pole figures of α-Zr matrix and δ-hydrides (δ-$ZrH_{1.66}$). Squares in different colors distinguish the projected points of α-Zr matrix and δ-$ZrH_{1.66}$. Habit plane of δ-hydrides and cracking plane coincide with the same $\{10\bar{1}0\}$ prismatic plane in α-Zr.

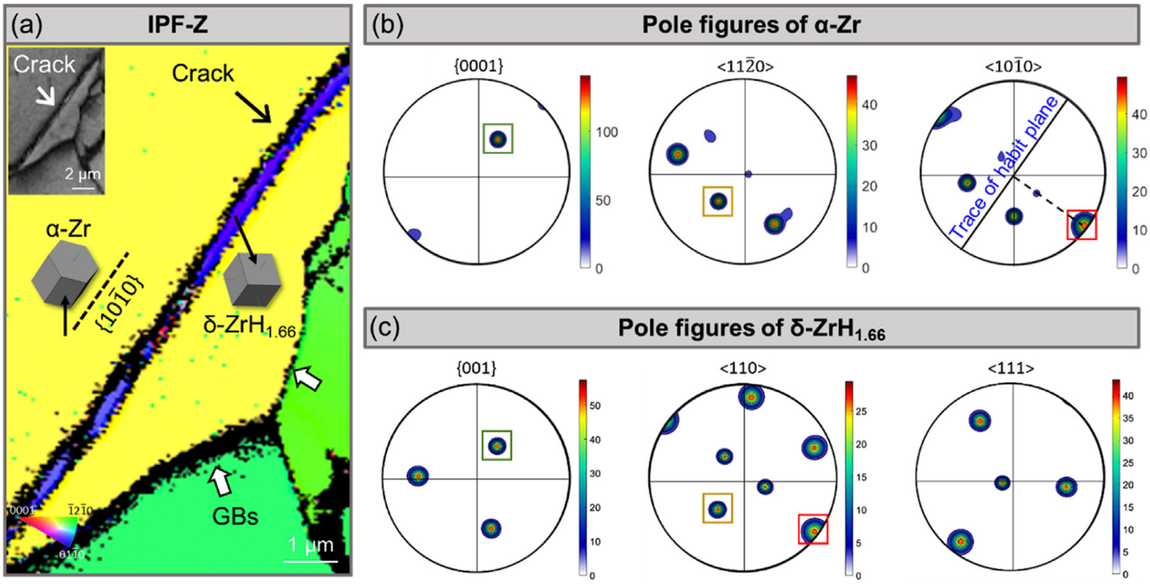

Fig. 6. Orientation relationship between the δ-hydrides and Zr matrix in hydrogenated pure Zr (Zr-H10). (a) Crystal orientation map (with step size of 0.02 μm) of an annealing crack and δ-hydrides. Band-contrast (BC) map that clearly reveals the cracking morphology inside the grain is inserted in the top left. (b) and (c) Pole figures of α-Zr matrix and δ-hydrides (δ-ZrH$_{1.66}$). Squares in different colors indicate the superposed projection points of α-Zr matrix and δ-ZrH$_{1.66}$. The habit plane of δ-hydrides and cracking plane both lie along the same $\{10\bar{1}0\}$ prismatic plane in α-Zr.

with a (0001) habit plane as *basal hydrides*. In Zr, the basal plane is not the preferred cleavage plane, but the prismatic $\{10\bar{1}0\}$ plane is [28]. This may explain why δ-hydrides, which are commonly basal hydrides, are not crack initiators. Closer analysis reveals that not only do the annealing cracks propagate parallel to the prismatic δ-hydride bundles, but they also form along the $\{10\bar{1}0\}$ planes (see Fig. 4(c), (f), and Fig. 5(a), and supplementary material, Fig. S2). The results suggest that prismatic-plane microcrack paths for both intra- and intergranular annealing cracks are a signature of prismatic δ-hydride formation.

As mentioned, basal δ-hydrides are common in Zr with certain hydrogen concentration and are not anticipated to cause cracking under annealing. To affirm that the annealing cracking observed here is unusual, analysis was repeated under a slightly hydrogen-rich environment. We further increased the initial hydride concentration via electrolytic hydrogen charging [5] to either 20 or 43 wppm (Table 3), and then annealed following the same procedures in Table 4. Supplementary material, Fig. S4 compares the characteristics of the cracks formed in the Zr-H10 sample containing 20 wppm hydrogen and Zr-H30 sample containing 43 wppm hydrogen with the as-received pure Zr (denoted as AR-Zr). Annealing cracks also formed in the hydrogen-charged Zr samples after annealing. The number density of cracks in the hydrogen-charged Zr samples increases with hydrogen concentration, which is expected. The annealing cracking in the hydrogen-charged Zr samples (Zr-H10) (Fig. 6) have many crystallographic characteristics in common with uncharged Zr. The cracks are transgranular and propagate along the $\{10\bar{1}0\}$ prismatic planes (Fig. 6(a)). As can be seen, they are connected to δ-hydride bundles. With the Zr matrix, the δ-hydrides also adopt an OR of $(0001)_{\alpha\text{-Zr}}//\{001\}_{\delta}$, $<11\bar{2}0>_{\alpha\text{-Zr}}//<110>_{\delta}$ and $<10\bar{1}0>_{\alpha\text{-Zr}}//<110>_{\delta}$ (Fig. 6(b) and (c)) and have a $\{10\bar{1}0\}$ habit plane and hence are prismatic hydrides (indicated by black line in $<10\bar{1}0>_{\alpha\text{-Zr}}$ pole figure).

Fig. 7 shows the TEM evidence for crack initiation at the prismatic δ-hydrides and not at the basal δ-hydrides. Fig. 7(a) shows an area including the $\{10\bar{1}0\}$ fracture plane of the cracked grain (Grain A) and uncracked neighboring grain (Grain B), extracted by a FIB lift-out technique (the lift-out area is marked in Fig. 7(a)). Fig. 7(b) is a low magnification bright-field (BF) TEM image of the area. Abundant hydride platelets are observed in both Grains A and B. Fig. 7(c) and (d) shows diffraction patterns of the white circled regions in Fig. 7(b). The δ-hydrides in cracked Grain A are prismatic hydrides and assume the OR of $(0001)_{\alpha\text{-Zr}}//\{001\}_{\delta}$, $<11\bar{2}0>_{\alpha\text{-Zr}}//<110>_{\delta}$ and $<10\bar{1}0>_{\alpha\text{-Zr}}//<110>_{\delta}$, which is consistent with the EBSD results (Fig. 7(d)). The OR obtained from the diffraction pattern in Fig. 7(d) further confirms the formation of prismatic δ-hydrides in the cracked grain (Grain A). Fig. 7(f) shows a dark-field (DF) TEM image of these prismatic δ-hydrides by selecting a $(\bar{2}00)_{\delta}$ spot in Fig. 7(d). As shown in Fig. 7(f), δ-hydrides have an irregular shape, unlike that usually reported for δ-hydrides [29]. The analysis confirms that they lie on the $\{10\bar{1}0\}$ habit plane. The δ-hydrides in the uncracked Grain B, however, are basal hydrides and adopt an OR of $(0001)_{\alpha\text{-Zr}}//\{111\}_{\delta}$ and $<11\bar{2}0>_{\alpha\text{-Zr}}//<110>_{\delta}$ with the Zr matrix (Fig. 7(c)). Further analysis in Fig. 7(c) reveals that they have a twinned structure with a $\{\bar{1}11\}$ twinning plane. For completeness, Fig. 7(e) is the DF-TEM image of these basal hydrides, showing that they have the characteristic needle-liked shape when viewing along the $[2\bar{1}\bar{1}0]$ direction [29]. The more familiar basal δ-hydride are not crack initiators.

For the annealed Zr-Sn-Nb-Fe (Type-II) alloy, the δ hydrides are also prismatic, yet the hydride/Zr interface has a different OR than that of the pure Zr (Fig. 8). Nonetheless, annealing cracks initiate at prismatic δ-hydrides and propagate along a crystallographic $\{10\bar{1}0\}$ prismatic path of these hydrides (Fig. 4(c) and (f), and Fig. 8(a)).

4. Discussion

4.1. Cooling rate-dependent hydride variants selection and cracking

The precipitation of hydride is a complex process. With a constant hydrogen concentration, the selection of hydride variants mainly depends on the cooling rate [26,30,31]. Several experimental studies including electron metallography [26,30,32], dilatometry [33], and X-ray diffraction [32,33] show that formation of δ-hydride is favored by slow cooling, while γ-hydride is commonly observed after quenching. The γ-hydride is a metastable phase that usually is produced via martensitic transformation involving coordinated atomic shear motion [28], while the δ-hydride

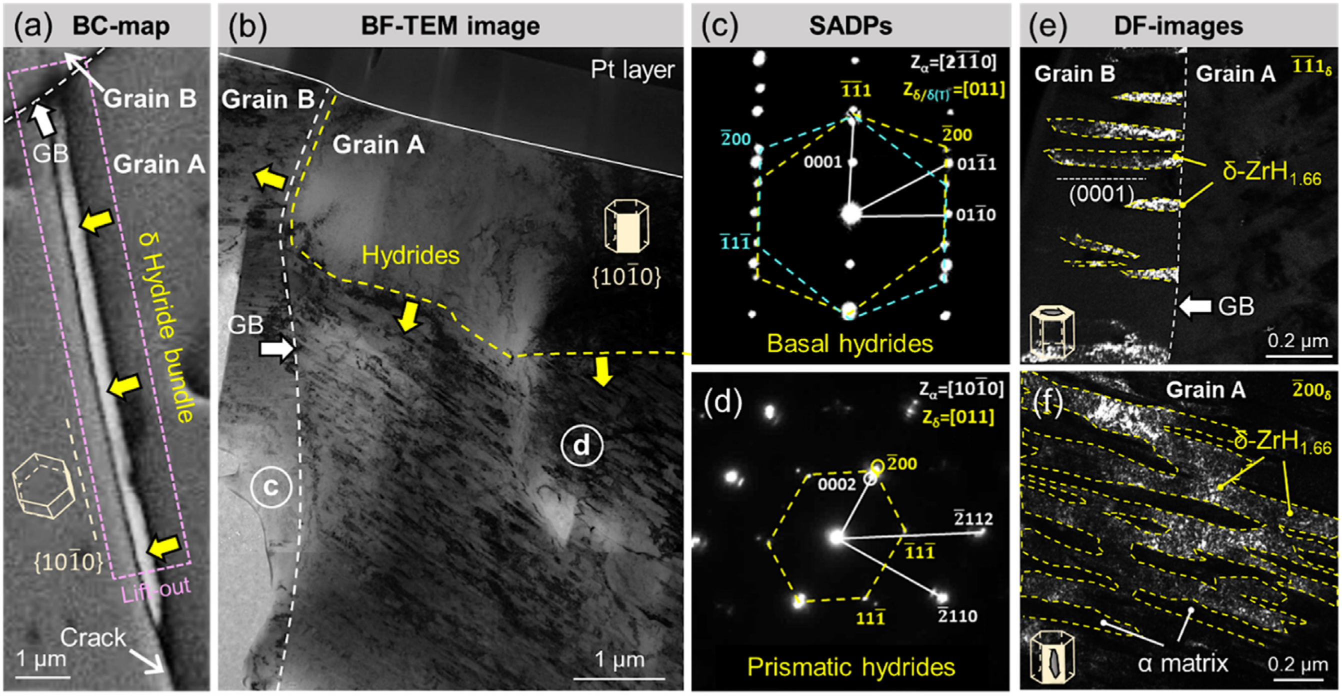

Fig. 7. Prismatic and basal δ-hydrides. (a) Location for TEM foil cutting. The crack is in Grain A, while there is no crack in adjacent Grain B. The δ-hydrides and Zr matrix are shown in BC map. (b) Bright-field (BF) TEM image of the lift-out area in (a). (c) and (d) Diffraction patterns obtained from the white circles in (b). (e) and (f) Dark-field (DF) images of the δ-hydrides viewed along ($\bar{1}\bar{1}$1) in (c) and ($\bar{2}$00) in (d), respectively. Hydrides are highlighted by yellow dash lines.

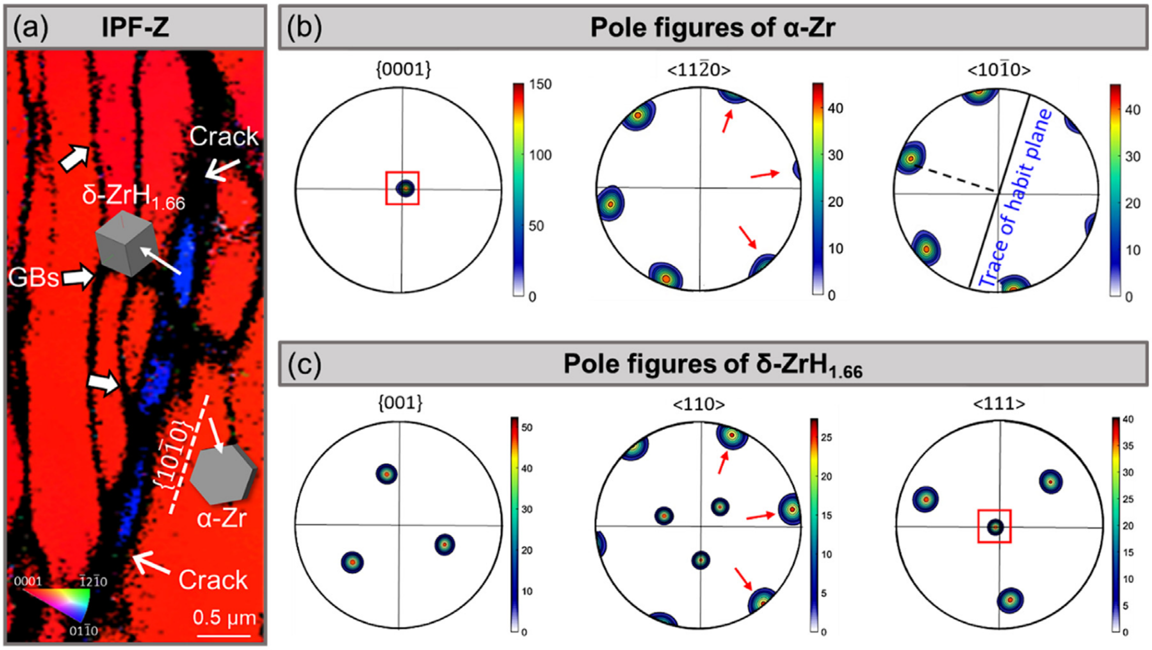

Fig. 8. Orientation relationship between the δ-hydrides and Zr-Sn-Nb-Fe alloy (Type-II) matrix across several grains. (a) Crystal orientation map (with step size of 0.02 μm) of an annealing crack and hydrides corresponding to the cracked region in Fig. 4(c). (b) and (c) Pole figures of the α-Zr matrix and δ hydrides (δ-$ZrH_{1.66}$). Red squares and arrows in pole figures indicate the superposed projection points of α-Zr matrix and δ-$ZrH_{1.66}$. Habit planes of individual δ hydrides and cracking plane lie along the same {10$\bar{1}$0} prismatic plane in α-Zr.

is an equilibrium phase usually formed via diffusional phase transformation [27]. The dilatational strain associated with δ-hydride (+17.2 %) is significantly larger than that for γ-hydride (+12.3 %) [27]. This can explain the longer times required to form equilibrium δ-hydrides and need for slow cooling conditions.

According to conventional thought, the formation of δ-hydrides in light hydrogen concentration and stress-free environments are not linked to crack initiation. In the absence of stress, δ-hydrides preferentially precipitate on the basal plane of the Zr matrix, where the lattice mismatch (i.e., misfit) is low [14–18,27]. In congruence, we show that basal plane δ-hydrides are not crack initiators (Fig. 7). They also do not participate in crack propagation. As we have shown, cracking, nonetheless, occurs in hydrogen-dilute Zr and Zr-Sn-Nb-Fe alloy during annealing, a stress-free, cooling

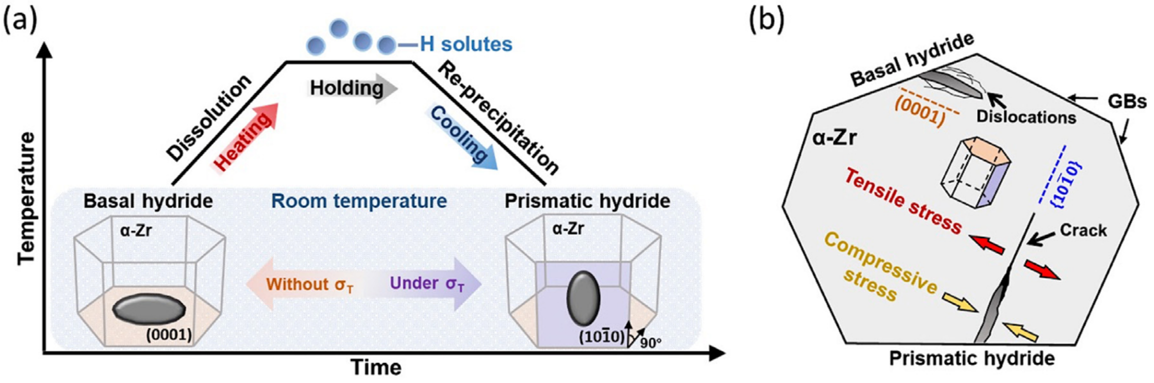

Fig. 9. Schematics of stress-induced δ-hydride reorientation and crack initiation. (a) Reorientation of hydride habit plane from basal to prismatic is induced by intergranular thermal tensile stress (denoted as σ_T) during cooling process. Hydrogen solutes are marked with blue dots. (b) Precipitation of prismatic hydride induces tensile stress on the Zr matrix, which subsequently triggers cleavage cracking along the prismatic plane. Basal hydrides that precipitate without tensile stress or under compressive stress are safer.

Table 5
Dilatational misfits associated with basal and prismatic δ-hydride formation along specified crystallographic directions.

Hydride type	Orientation relationship	$[utvw]_\alpha$	$[uvw]_\delta$	$\delta_{[uvtw]}$ (%)
Basal δ-hydride	$(0001)_\alpha//\{111\}_\delta$	[0001]	[111]	+7.25%
	$<11\bar{2}0>_\alpha//<110>_\delta$	$[11\bar{2}0]$	[110]	+4.76%
		$[1\bar{1}00]$	[112]	+4.58% [21]
Prismatic δ-hydride	$(0001)_\alpha//\{001\}_\delta$	[0001]	[001]	−7.10% [21,36]
	$<11\bar{2}0>_\alpha//<110>_\delta$	$[11\bar{2}0]$	[110]	+4.76%
	$<10\bar{1}0>_\alpha//<110>_\delta$	$[10\bar{1}0]$	$[0\bar{1}1]$	+20.70% [36]

step from elevated temperature at a slow rate (Fig. 9(a)). Analysis of this unexpected annealing cracking, in Zr and Zr-Sn-Nb-Fe alloys alike, point to the precipitation of an uncommon prismatic δ-hydrides as the origin of the cracking. Further, crack propagation occurs along the $\{10\bar{1}0\}$ prismatic plane, where prismatic δ-hydrides lie (Fig. 9(b)). Thus, contrary to popular belief, the stress-free, furnace cooling at a slow rate can in fact be detrimental for Zr. This explains why WQ is unexpectedly seen here to thwart formation of δ-hydrides and leave the material crack-free.

4.2. Precipitation of basal and prismatic hydrides

We address the clear preference for crack initiation from prismatic δ-hydrides over basal hydrides. The volume expansion associated with hydride formation causes a compressive strain in the hydride and tensile strain in the surrounding Zr matrix (Fig. 9(b)) [34,35]. The mismatch of lattice parameters between the δ-hydride and surrounding α-Zr is anisotropic [21,27,36]. The transformation of the α-Zr to the δ-hydride is accomplished by a simple expansion of the atomic lattice on its habit planes. The misfit strain between the δ-hydride and the α-Zr matrix along a direction $[uvtw]_\alpha$ is given by: $\delta_{[uvtw]} = (d_\delta - d_\alpha)/d_\alpha$, where d_δ and d_α are the interplanar spacings of corresponding planes in the δ-hydride and α-Zr matrix [27]. The dilatational misfits between basal δ-hydrides and prismatic δ-hydrides along different directions are listed in Table 5 [21,36]. For basal δ-hydrides with a $(0001)_\alpha//\{111\}_\delta$, $<11\bar{2}0>_\alpha//<110>_\delta$ OR, the expansion strain on the basal plane along $[0001]_\alpha$ c-axis is +7.25 % (i.e., $d_\alpha = 0.257$ nm, $d_\delta = 0.276$ nm, which makes the value of $\delta_{[0001]} = +7.25$ %). Tensile strains generated by basal δ-hydrides are relieved by dislocation emissions from the hydride-matrix interface [37]. Therefore, the strains generated in this case are suspected to be sufficiently low that they could be relieved by dislocation emission from the hydride-matrix interface (indicated by basal hydride shown in Fig. 9(b)) [37]. For prismatic δ-hydrides with an OR of $(0001)_\alpha//\{001\}_\delta$, $<11\bar{2}0>_\alpha//<110>_\delta$ and $<10\bar{1}0>_\alpha//<110>_\delta$, the misfit strains are −7.10 % along $[0001]_\alpha$ (i.e., $d_\alpha = 0.257$ nm, $d_\delta = 0.239$ nm, $\delta_{[0001]} = -7.10$ %) and +20.70 % along $[10\bar{1}0]_\alpha$ (i.e., $d_\alpha = 0.140$ nm, $d_\delta = 0.169$ nm, $\delta_{[10\bar{1}0]} = 20.70$ %). Compared to basal hydrides with minimized strain accommodation energy, the rather larger strain generated by the precipitation of prismatic δ-hydrides can directly lead to cleavage cracking along the $\{10\bar{1}0\}$ prismatic plane, the intrinsically weakest plane in Zr [28]. Prismatic δ-hydrides can be more detrimental as crack initiators than basal δ-hydrides (Fig. 9(b)).

4.3. Intergranular thermal stress-stimulated prismatic δ-hydride

An important question that remains concerns the formation of prismatic δ-hydrides over the common basal δ-hydrides. Without an external stress, δ-hydrides preferentially precipitate on the Zr basal plane. Reorientation to one of several other possible habit planes, $\{10\bar{1}i\}$ planes, where $i = 0$–7, including the prismatic plane, requires external stress [19–21]. The threshold stress expected for hydride cluster reorientation is around 100 MPa [21,38]. Since no external load is applied while annealing in this study, prismatic δ-hydrides likely formed because of intergranular thermal residual stresses introduced during annealing. In principle, the significant anisotropy in thermal expansion coefficients along $\langle a\rangle$ axis ($\alpha_a = 5.8 \times 10^{-6}$ K^{-1}) and $\langle c\rangle$ axis ($\alpha_c = 10.3 \times 10^{-6}$ K^{-1}) could cause intergranular thermal residual stresses on the order of 100 MPa during slow cooling [39–41]. For a single grain, the (0002) grains will be under tension and $\{10\bar{1}0\}$ grains under compression [39]. The residual stresses will be more intense at the GBs and triple junctions, where the mismatch in thermal distortions at two or more misoriented grains must maintain the compatibility. Two experimental studies have confirmed intergranular residual stress development during cooling from annealing in Zr. Using neutron diffraction, MacEwen et al. determined the residual strains produced during cooling of Zircaloy-2 [39]. They found that slow cooling from 900 K introduces residual stresses of the order of 100 MPa. In addition, Luan et al. reported that annealing twin-

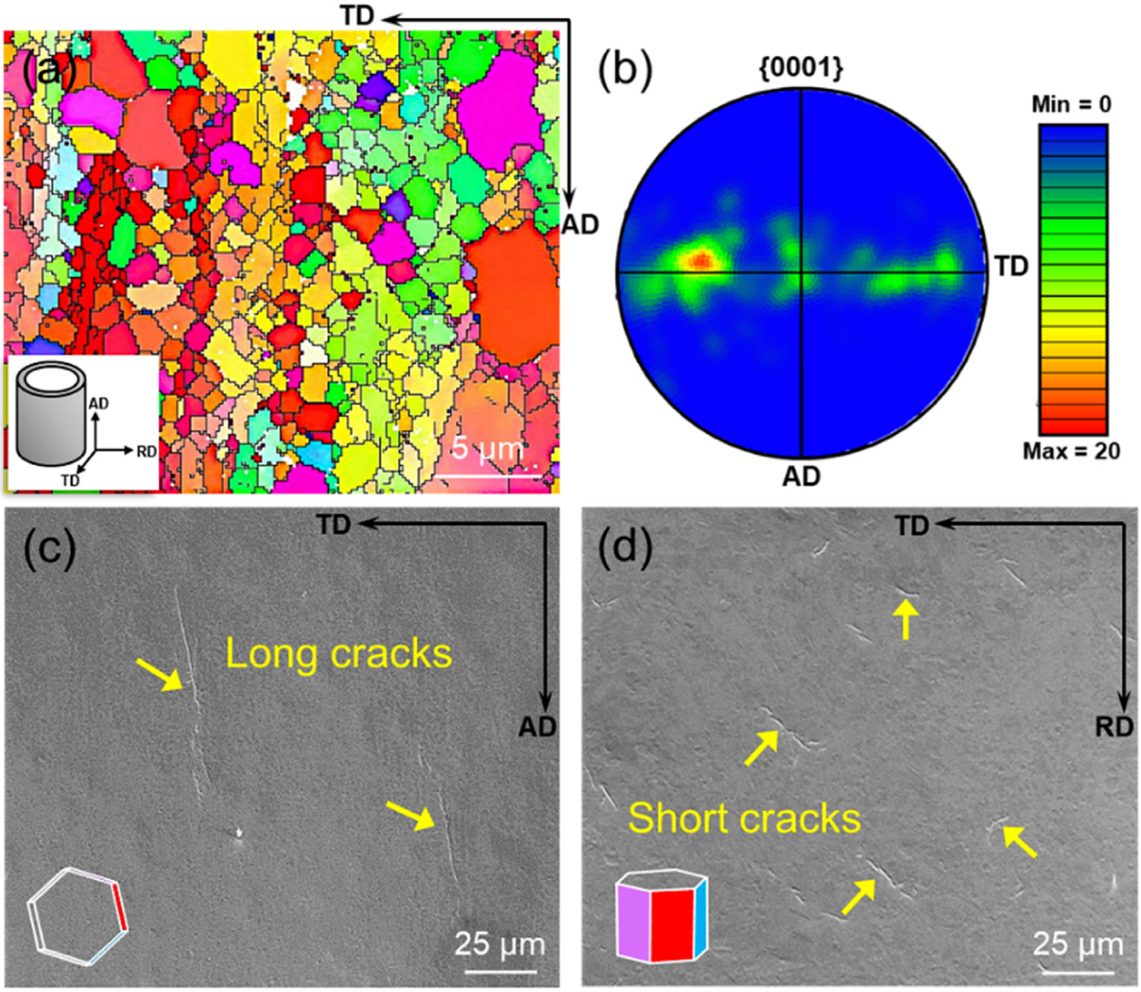

Fig. 10. Effect of texture on annealing cracking. (a) IPF map showing common grain orientations on the TD-AD plane of Type-II Zr-Sn-Nb-Fe alloy. The inset is a schematic of the Z-Sn-Nb-Fe tube sample. (b) {0001} basal pole figure showing the bimodal basal texture of the Zr-Sn-Nb-Fe tube. (c) and (d) Cracking microstructures on the TD-AD and TD-RD planes under the same magnification. Cracks on the former plane are long and straight, while cracks on the latter plane are shorter and bent.

ning is induced by such an intergranular thermal residual stress after $\beta\rightarrow\alpha$ furnace cooling [41]. In this study, reprecipitation of δ-hydrides on the prismatic plane is argued to occur predominantly at the GBs and under intergranular thermal residual stress generated in cooling, see schematic in Fig. 9(a). This would also explain why the prismatic δ-hydride bundles are thicker at the GBs than grain interior. The observed crack number density gradient along the bundle thickness is related to the stress state difference within the sample interior and at the subsurface, where crack nucleation is easier (supplementary material, Fig. S1) [27,28].

4.4. Crack initiating mechanism

The conventional thought on delayed hydride cracking (DHC) observed in Zr cladding tubes involves a sub-critical crack growth mechanism, wherein crack propagation occurs through the growth and fracture of precipitated hydrides at a pre-existing crack-tip under an applied tensile stress [4,5,42–44]. To our knowledge, the only available studies concerning DHC involve high-hydrogen concentrations (usually more than 50 wppm) [4,43]. Further, as mentioned, DHC has been linked to hydrides with a certain *morphological* orientation [43,44]; radial hydrides are also more susceptible to hoop stresses in the tube (generated from nuclear fuel expansion) than circumferential hydrides, and serve as channels for crack propagation [6]. A connection to hydride crystallography or detailed explanation for how cracks would initiate from these hydrides has not been put forth. Unlike the proposed DHC process, the mechanism underlying the annealing cracking seen here is directly initiated by hydrides with a certain crystallographic orientation and occurs with dilute hydrogen concentrations ($<$50 wppm) and no external stress. These crack initiating sites are prismatic δ-hydrides, whose presence is unexpected.

4.5. Strategies to retard hydride cracking

Analysis here reveals that incipient cracks initiated by δ-hydride bundles have a preferential crystallographic pathway, specifically following the $\{10\bar{1}0\}$ prismatic planes of Zr grains (see an example of a zigzag crack in supplementary material, Fig. S5). As shown in Fig. 4(c) and (f), cracks propagate continuously along the prismatic planes in neighboring grains with similar orientations in textured Zr–Sn–Nb–Fe alloys. Long, interlinked crack formation across GBs is, therefore, can in part be attributed to the strong texture in the Zr alloy components inherited from thermomechanical processing [14]. Such crack linking can be impeded by weakening the texture. With a weak texture, the distribution of prismatic planes in different grains is random, and cracks stop at GBs. To test the feasibility of altering the texture to suppress cracking, we repeated the annealing for different orientations of Zr–Sn–Nb–Fe sample and studied the extent of cracking (Fig. 10). The analysis presented in Fig. 10 finds that cracks propagate continuously along the prismatic planes in neighboring grains with similar orientations (Fig. 10(c)), but impeded at GBs of grains with different orientations (Fig. 10(d)). The former case would represent the strongly textured material, typically found in the Zr cladding tube, and the latter case the proposed situation with a weak texture.

Last, based on the insights gained on the origin of annealing cracking, two strategies for retarding cracking are offered. The first recommends that even in an external stress-free environment, an ultra-fast cooling during heat treatment, such as WQ, is paramount for the hydrogen-dilute Zr components (Fig. 2(d)). Rapid cooling impedes the precipitation of δ-hydrides, while γ-hydrides may precipitate during quenching (supplementary material, Fig. S3) [30,31]. γ-hydrides are fine, randomly distributed, and tend not to promote cracking. This strategy can be readily incorporated in the industrial fabrication process of Zr alloy products. The second strategy suggests weakening the texture of Zr alloy products. The texture control method can be used in the processing of industrial grade Zr alloys used in chemical engineering applications. Altering the typical bimodal basal texture in Zr-Sn-Nb-Fe for cladding tubes would, however, call for changing current industrial cladding forming practices and is not as easily implemented as the first strategy [45].

5. Conclusion

We report an unexpected annealing crack initiating mechanism in pure Zr and Zr-Sn-Nb-Fe alloys that involves precipitation of the thermal intergranular stress induced prismatic δ-hydrides. The δ-hydrides on prismatic plane produce localized expansion stresses that trigger cleavage cracking along it. Unlike the common basal δ-hydrides, these prismatic δ-hydrides serve as crack initiators. Since intermediate annealing or recrystallization annealing is an indispensable step for processing, cracks induced by prismatic δ-hydrides during slow cooling may have formed in as-manufactured Zr components and are likely to be the cause of poor formability of Zr products and may also be the source of cracks in DHC. The findings here not only reveal an underlying crack initiating mechanism of hydrogen embrittlement, but also provide potential industrial processing routes for high quality Zr products.

Declaration of Competing Interest

The hydride cracking suppressing technology has been patented (CN ZL202110627439.7).

Acknowledgments

The authors benefit discussion with Prof. Zhi-Wei Shan and Dr. Si-Mian Liu and appreciate Dr. Qiang Yue for providing the samples. This work was supported by the National Natural Science Foundation of China (Nos. 51922082 and 51971170) and the 111 Project of China (Grant Number 2.0, BP0618008).

Supplementary materials

Supplementary material associated with this article can be found, in the online version, at doi:10.1016/j.jmst.2023.09.039.

References

[1] S. Lynch, Corros. Rev. 30 (2012) 105–123.
[2] Y.-S. Chen, H. Lu, J. Liang, A. Rosenthal, H. Liu, G. Sneddon, I. McCarroll, Z. Zhao, W. Li, A. Guo, J.M. Cairney, Science 367 (2020) 171–175.
[3] J.J. Kearns, J. Nucl. Mater. 22 (1967) 292–303.
[4] C.J. Simpson, C.E. Ells, J. Nucl. Mater. 52 (1974) 289–295.
[5] D.O. Northwood, U. Kosasih, Int. Mater. Rev. 28 (1983) 92–121.
[6] S.-J. Min, M.-S. Kim, K.-T. Kim, J. Nucl. Mater. 441 (2013) 306–314.
[7] A.T. Motta, L. Capulongo, L.Q. Chen, M.N. Cinbiz, M. Daymond, D.A. Koss, E. Lacroix, G. Pastore, P.C. Simon, M. Tonks, J. Nucl. Mater. 518 (2019) 440–460.
[8] R.S. Daum, S. Majumdar, Y. Liu, M.C. Billone, J. Nucl. Sci. Technol. 43 (2006) 1054–1067.
[9] H.C. Chu, S.K. Wu, K.F. Chien, R.C. Kuo, J. Nucl. Mater. 362 (2007) 93–103.
[10] M.L. Saux, J. Besson, S. Carassou, C. Poussard, X. Averty, Eng. Fail. Anal. 17 (2010) 683–700.
[11] J.-S. Kim, T.-H. Kim, D.-H. Kook, Y.-S. Kim, J. Nucl. Mater. 456 (2015) 235–245.
[12] J.R. Choubey, M.P. Puls, Metall. Mater. Trans. A 25 (1994) 993–1004.
[13] J. Li, M. Li, B. Guan, Y. Xin, Y. Wu, X. Liu, G. Chen, Int. J. Plast. 159 (2022) 103440.
[14] K. Une, K. Nogita, S. Ishimoto, K. Ogata, J. Nucl. Sci. Technol. 41 (2004) 731–740.
[15] K. Une, S. Ishimoto, J. Nucl. Mater. 357 (2006) 147–155.
[16] N.A.P. Kiran Kumar, J.A. Szpunar, Mater. Sci. Eng. A 528 (2011) 6366–6374.
[17] W. Qin, N.A.P. Kiran Kumar, J.A. Szpunar, J. Kozinski, Acta Mater. 59 (2011) 7010–7021.
[18] S. Wang, F. Giuliani, T.B. Britton, Acta Mater. 169 (2019) 76–87.
[19] V. Perovic, G.C. Weatherly, S.R. MacEwen, M. Leger, Acta Metall. Mater. 40 (1992) 363–372.
[20] N.A.P. Kiran Kumar, Hydride Formation in Zirconium Alloys Ph.D. Thesis, University of McGill, 2011.
[21] Y.-J. Jia, W.-Z. Han, Acta Mater. 235 (2022) 118100.
[22] M. Hanlon, S.Y. Persaud, F. Long, A. Korinek, M.R. Daymond, J. Nucl. Mater. 515 (2019) 122–134.
[23] T.P. Earle, J.S. Robinson, J.J. Colvin, J. Mater. Process. Technol. 153-154 (2004) 330–337.
[24] X.Y. Liu, C.J. McMahon, Mater. Sci. Eng. A 499 (2009) 540–541.
[25] K. Une, S. Ishimoto, J. Nucl. Mater. 322 (2003) 66–72.
[26] J.S. Bradbrook, N. Ridley, G.W. Lorimer, J. Nucl. Mater. 42 (2) (1972) 142–160.
[27] G.J.C. Carpenter, J. Nucl. Mater. 48 (1973) 264–266.
[28] S.-M. Liu, S.-H. Li, W.-Z. Han, J. Mater. Sci. Technol. 35 (2019) 1466–1472.
[29] Y.-J. Jia, I.J. Beyerlein, W.-Z. Han, Acta Mater. 216 (2021) 117146.
[30] B. Nath, G.W. Lorimer, N. Ridley, J. Nucl. Mater. 58 (1975) 153–162.
[31] R. Birch, S. Wang, V.S. Tong, T.B. Britton, J. Nucl. Mater. 513 (2019) 221–225.
[32] F. Long, Y. Luo, O. Shiman, M. Topping, S.Y. Persaud, Z. Yao, L.K. Beland, M.R. Daymond, Acta Mater. 221 (2021) 117369.
[33] B.J. Gill, J.E. Bailey, P. Cotterill, J. Less-Common Met. 40 (1975) 129–138.
[34] S.-M. Liu, A. Ishii, S.-B. Mi, S. Ogata, J. Li, W.-Z. Han, Small 51 (2021) 2105881.
[35] O. Zanellato, M. Preuss, J.Y. Buffiere, F. Riberiro, A. Steuwer, J. Desquines, J. Andrieux, B. Krebs, J. Nucl. Mater. 420 (2012) 537–547.
[36] F. Long, D. Kerr, G. Domizzi, Q. Wang, M.R. Daymond, Acta Mater. 129 (2017) 450–461.
[37] H. Tummala, L. Capolungo, C. Tomé, J. Nucl. Mater. 511 (2018) 406–416.
[38] J.-S. Kim, Y.-J. Kim, D.-H. Kook, Y.-S. Kim, J. Nucl. Mater. 456 (2015) 246–252.
[39] S.R. MacEwen, C. Tome, J. Faber, Acta Metall. 37 (1989) 979–989.
[40] T.M. Holden, R.A. Holt, J.W.L. Pang, Metall. Mater. Trans. A 33 (2002) 749–755.
[41] B.F. Luan, L.J. Chai, G.L. Wu, H.B. Yu, J.W. Chen, Q. Liu, Scr. Mater. 67 (2012) 716–719.
[42] R.N. Singh, N. Kumar, R. Kishore, S. Roychaudhury, B.P. Kashyap, J. Nucl. Mater. 304 (2002) 189–203.
[43] C.D. Cann, E.E. Sexton, Acta Mater. 28 (1980) 1215–1221.
[44] Y.S. Kim, S.B. Ahn, Y.M. Cheong, J. Alloys Compd. 429 (2007) 221–226.
[45] Y.J. Jia, W.Z. Han, Materials (Basel) 16 (2023) 2419.